Metal Fabrication by Additive Manufacturing Using Laser and Electron Beam Melting Technologies

ARTICLE *in* JOURNAL OF MATERIALS SCIENCE AND TECHNOLOGY -SHENYANG- · JANUARY 2012

Impact Factor: 1.61 · DOI: 10.1016/S1005-0302(12)60016-4

9 AUTHORS, INCLUDING:

Lawrence Murr
University of Texas at El Paso
476 PUBLICATIONS **7,024** CITATIONS
SEE PROFILE

Edwin Martinez
University of Texas at El Paso
35 PUBLICATIONS **366** CITATIONS
SEE PROFILE

Krista N Amato
12 PUBLICATIONS **122** CITATIONS
SEE PROFILE

Francisco Medina
University of Texas at El Paso
90 PUBLICATIONS **761** CITATIONS
SEE PROFILE

Available online at www.sciencedirect.com
ScienceDirect
J. Mater. Sci. Technol., 2012, **28**(1), 1–14.
JMST
www.JMST.org

• *Invited Review*

Metal Fabrication by Additive Manufacturing Using Laser and Electron Beam Melting Technologies

Lawrence E. Murr[1,2)†], *Sara M. Gaytan*[1,2)], *Diana A. Ramirez*[1,2)], *Edwin Martinez*[1,2)], *Jennifer Hernandez*[1,2)], *Krista N. Amato*[1,2)], *Patrick W. Shindo*[1,2)], *Francisco R. Medina*[1,2)] *and Ryan B. Wicker*[1,2)]

1) Department of Metallurgical and Materials Engineering, The University of Texas at El Paso, El Paso, TX 79968, USA
2) W.M. Keck Center for 3D Innovation, The University of Texas at El Paso, El Paso, TX 79968, USA

[Manuscript received October 27, 2011]

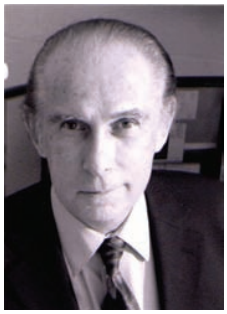

Lawrence E. Murr is Mr. & Mrs. MacIntosh Murchison Professor and Chairman of the Department of Metallurgical and Materials Engineering and Ph.D. Program Director in the Materials Research & Technology Institute at The University of Texas at El Paso. Dr. Murr received his B.Sc. in physical science from Albright College, and his B.S.E.E. in electronics, his M.S. in engineering mechanics, and his Ph.D. in solid-state science, all from the Pennsylvania State University. Dr. Murr has published 20 books, over 750 scientific and technical articles in a wide range of research areas in materials science and engineering, environmental science and engineering, manufacturing science and engineering (especially rapid prototype/layered manufacturing), and biological sciences and engineering; roughly half with undergraduate and graduate student researchers. During more than 45 years of university teaching, Professor Murr has also directed 65 M.S. theses and 35 Ph.D. dissertations. Recent honors include the 2001 Buehler Technical Paper Merit Award for Excellence (IMS), the TMS 2007 Educator Award, the 2007 John S. Rinehart Award (a TMS Symposium Award for global leadership in shock and high-strain-rate phenomena), and the 2008 Henry Clifton Sorby Award presented by the International Metallographic Society (IMS) for recognition of lifetime achievement in the field of metallurgy. In 2009, Professor Murr received the Albert Easton White Distinguished Teacher Award from ASM International. Dr. Murr was also awarded a Lee Hsun Research Award by the Shenyang National Laboratory for Materials Science, Institute of Metal Research, Chinese Academy of Sciences (IMR-CAS) "in recognition of past accomplishments in materials science and technology" (2009–2010). In 2010, Professor Murr was honored as a Visiting Professor for Senior International Scientists by the Chinese Academy of Sciences (CAS) for the Institute of Metal Research (IMR) of the Shenyang National Laboratory (SYNL) for Materials Science. Also in 2010, Professor Murr was appointed as the Guest Professor of Harbin Engineering University. Professor Murr was chosen for a Piper Professor of 2010 Award for "Outstanding scholarly achievements and superior teaching at the college level", a Texas higher education program of the Minnie Stevens Piper Foundation. Professor Murr is a member of the International Advisory Board for Journal of Materials Science & Technology, and the Founding Advisory Board of Metallography, Microstructures & Analysis. Professor Murr is a Fellow of ASM International and a licensed professional engineer. He holds 3 patents and has 1 pending.

† Corresponding author. Prof., Ph.D.; E-mail address: lemurr@utep.edu (L.E. Murr).

Selective laser melting (SLM) and electron beam melting (EBM) are relatively new rapid, additive manufacturing technologies which can allow for the fabrication of complex, multi-functional metal or alloy monoliths by CAD-directed, selective melting of precursor powder beds. By altering the beam parameters and scan strategies, new and unusual, even non-equilibrium microstructures can be produced; including controlled microstructural architectures which ideally extend the contemporary materials science and engineering paradigm relating structure-properties-processing-performance. In this study, comparative examples for SLM and EBM fabricated components from pre-alloyed, atomized precursor powders are presented. These include Cu, Ti–6Al–4V, alloy 625 (a Ni-base superalloy), a Co-base superalloy, and 17-4 PH stainless steel. These systems are characterized by optical metallography, scanning and transmission electron microscopy, and X-ray diffraction.

KEY WORDS: Selective laser melting; Electron beam melting; Additive manufacturing; Microstructures; Microstructural architecture

1. Introduction

Although rapid prototyping (RP) and related layer manufacturing technologies involving solid freeform fabrication (SFF) have been variously developed over the past several decades, the recent availability of commercial systems utilizing both laser and electron beam melting have posed revolutionary manufacturing concepts. Indeed, Chuna *et al.*[1] have recently referred to this range of layer manufacturing as a "renaissance in manufacturing". In earlier developments, RP was used mostly for fabricating complex polymer prototypes which has now become well established[2–4]. More recent advances in metal component manufacturing using 3D solid models embedded in computer-aided design (CAD) software poses the prospect for layer-by-layer fabrication of complex, custom metal or alloy products impossible to achieve by more conventional processing of wrought or cast precursors[1,4]. Because the melting occurs in layers of pre-alloyed metal powders forming small melt volumes or melt pools which rapidly solidify, the resulting solid component microstructures can achieve unique, directional growth features far from equilibrium in a more conventional thermodynamic sense. Such multiscale, hierarchical structures or microstructures may provide possible routes for tailoring or optimizing metal properties and performance.

In this paper we review recent applications of laser and electron beam melting systems in the fabrication of metal and alloy components from pre-alloyed, atomized powders. These components include simple geometries, including various sizes of cylindrical and rectangular block products as well as more complex mesh and foam components which are especially novel because they can be fabricated in complex systems with high specific strength and stiffness. In addition, because relative density (ρ/ρ_o) and relative stiffness (E/E_o) are related, functional metal systems can be fabricated to achieve stiffness compability such as stress shielding reduction in orthopaedic alloy implants[5,6].

2. Comparison of Electron and Laser Beam Melting Systems

Fig. 1 shows simple schematic views for an electron beam melting (EBM) system (Fig. 1(a)) and a laser beam melting (LBM) system, popularly referred to as selective laser melting (SLM) (Fig. 1(b)). Corresponding EBM and SLM commercial systems have been made available since about 2005 by Arcam AB (Sweden) and EOS GmbH (Germany), respectively. Relevant results of research to be presented herein were obtained with either an Arcam A2 or similar EBM system, and an EOS M270 SLM system. These systems create a powder bed by raking or rolling powder fed from cassettes into a compacted layer usually several powder particles thick, which is then selectively melted by the scanned electron or laser beam, respectively as shown in Fig. 1(a) and (b). These powders are rapidly solidified or atomized in an insert environment such as purified argon and appear typically as shown in Fig. 1(c) for pure copper, and in Fig. 2 for a pre-alloyed Co-base superalloy powder (having a composition of Co-26Cr-6Mo-0.2C in weight percent). The magnified insert in Fig. 2 shows the microdendritic structure typical for rapidly solidified Co-base or Ni-base supealloy powders[7,8]. Spherical or near-spherical powders with a distribution of powder particle sizes (Figs. 1(c) and 2) are more optimized for efficient flow and layer packing, as well as melt uniformity.

In the EBM system in Fig. 1(a), electrons are generated in a gun (1) and accelerated with a 60 kV potential, focused using electromagnetic lenses (2), and electromagnetically scanned (3) by an embedded CAD program. The focused electron beam is initially scanned in multiple passes at a scan rate of $\sim 10^4$ mm/s with a high beam current ($\sim$30 mA) to preheat the powder bed to roughly 0.8 T_m (where T_m is the melting temperature). The final melt scan is reduced to a rate of $\sim 10^2$ mm/s and the beam current is also reduced to $\sim$5 to 10 mA. The beam scans x–y, and the final melt scan produces melt pools or

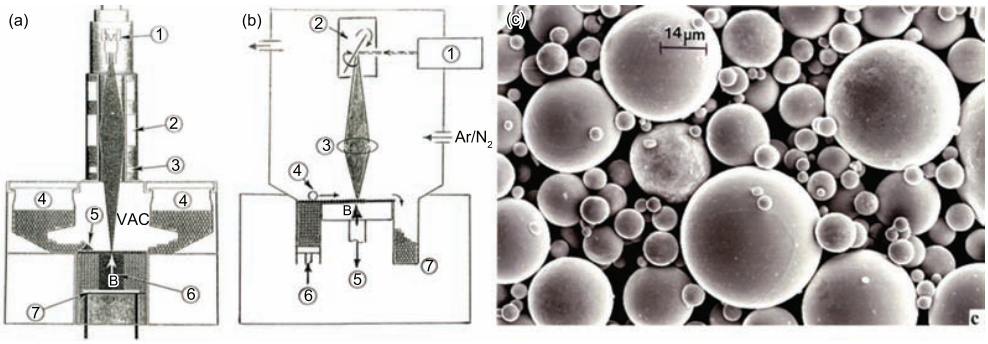

Fig. 1 EBM(a) and SLM (b) system schematics. Atomized Cu powder example; SEM image (c). See text for discussion of numbered system components

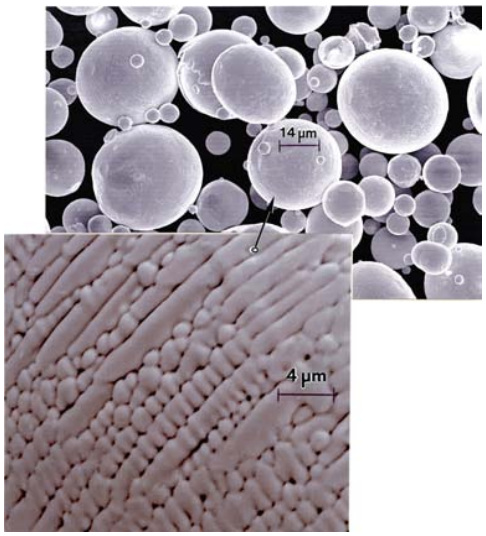

Fig. 2 Atomized Co-base, pre-alloyed precursor powder. SEM image. Insert shows magnified view of microdendritic structure

zones related to the beam diameter and scan spacing. The melt scan melts only selected layer areas as prescribed in the CAD model. In the EBM system shown schematically in Fig. 1(a), powder is gravity fed from cassettes (4) and raked (5) onto the build table (7) which is lowered with each successive layer building of the prescribed component (6). The corresponding build direction is denoted by the arrow at B in Fig. 1(a) which is in the z-direction relative to the x-y scanning of the powder layers. Mean or average powder particle sizes can range from ∼10 μm to 60 μm; with nominal sizes of ∼40 μm. Like any electron beam system, the EBM system operates under a vacuum of $<10^{-4}$ Torr. A helium gas bleed at the build area increases the pressure to $\sim 10^{-2}$ Torr but enhances heat conduction and component cooling.

In contrast to the EBM system, the SLM system in Fig. 1(b) utilizes a focused laser beam. The EOS M270 system utilizes a 0.2 kW Yb: YAG fiber laser (shown at (1) in Fig. 1(b)). The 100 μm diameter laser beam is scanned by a CAD driven rotating mirror system at (2) (Fig. 1(b)) and focused onto the powder bed at (B). A mechanical recoater (4) similar to the raking system in the EBM forms the powder layers onto the build platform (5). Powder is fed from a supply container at (6) in Fig. 1(b) while excess powder is collected for recycle at (7).

During the SLM build process, the build platform is heated to ∼90 °C and roughly maintained at this temperature, considerably cooler than the EBM build environment. The laser beam scans x–y between 800 and 1200 mm/s to form melt pool arrays similar to EBM melt scanning. Scanning can be in x–y in a layer or x or y in alternate layers. In the SLM, the EBM system vacuum is replaced by either purified Ar or nitrogen (N_2 or designated N2), which in addition to providing oxidation protection by purging the oxygen from the system, provides efficient heat conduction and component cooling. While the thermal conductivity for nitrogen gas is roughly 40% higher than argon up to 2000 K[9], there is usually no prominent variation in SLM component microstructures for most materials although the build cooling is consistently more rapid for SLM than EBM as noted. This is especially notable for small build volumes or component geometries for alloy systems with phase-sensitive thermodynamic regimes, *etc.* to be described below. It should also be noted that in addition to adjustments in beam scan speed, beam size (and energy density), scan spacing and related scan strategies, including directional or orthogonal scans (x–y), the melt scan can be repeated to remelt each layer. This allows for grain growth or other thermodynamic adjustments in the microstructure. In addition to multiple melt scans, the beam can also be adjusted to allow for re-heating of the layer in a process anneal.

3. Ti–6Al–4V Fabrication by EBM and SLM

Ti alloys have a wide range of applications in structural systems such as aeronautics or aerospace where light weight and especially high strength/weight ratios are required. Ti–6Al–4V in particular has been a popular alloy with a density of 4.43 g/cm^3, a specific

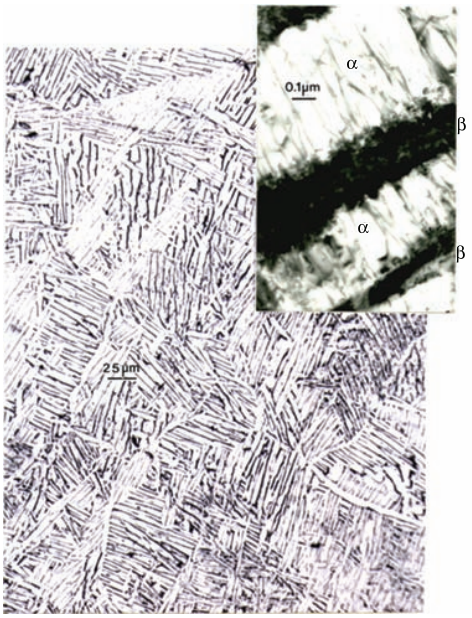

Fig. 3 Vertical section view (optical metallograph) for an EBM-fabricated Ti–6Al–4V cylindrical component showing acicular α-phase grains surrounded by interfacial β-phase (black). The TEM image insert shows high dislocation density in α-phase grains

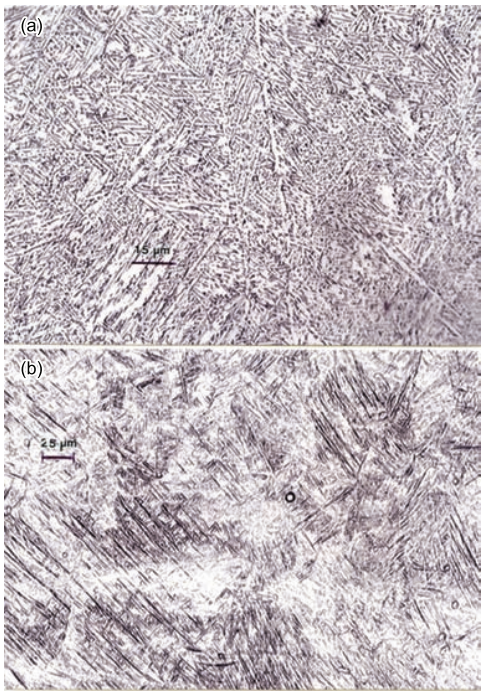

Fig. 4 Comparison of optical metallograph images for small volume, rapidly cooled Ti–6Al–4V components fabricated by EBM (a) and SLM (b). Note fine α-phase structure in (a) and dominant $\alpha\prime$-martensite plates in (b)

strength of 200 MPa/g/cm^3 and a melting point of ∼1650 °C. Ti–6Al–4V has also been popular as an orthopaedic joint replacement[10,11] although its elastic (Young′s) modulus or stiffness of 110 GPa is significantly greater than the hardest bone stiffness of 16 to 20 GPa[11,12]. The addition of Al and V to Ti increases the α (hcp)→β (bcc) phase transition temperature from 885 °C to 995 °C, while β-phase processing under strain (or β deformation) can create martensite (hcp α')[13].

Thijs *et al.*[14] have demonstrated that systematic manipulation of scanning strategies in the SLM processing of Ti–6Al–4V components can allow for variations in directional grain growth and microstructure, while Murr *et al.*[15] have demonstrated that SLM fabrication of Ti–6Al–4V components exhibits α' martensitic or α/α'microstructures in contrast to primarily α/β microstructures for EBM-fabricated Ti–6Al–4V components[16,17]. These microstructural features are illustrated on comparing Fig. 3, showing a vertical section view (parallel to the build direction) of acicular α-phase grains surrounded by β-phase interfacial regimes (dark) with a significantly reduced (finer) acicular α microstructure in Fig. 4(a) resulting for more rapid EBM product cooling; with a fine α'-martensitic microstructure in Fig. 4(b) for SLM fabrication. Figs. 3 and 4(a) show EBM microstructures for Ti-6Al-4V fabricated at higher beam current in a large volume component in contrast to reduced beam current fabrication of a much smaller volume component, respectively; resulting in cooling rate variations or increased solidification rates. The transmission electron microscope (TEM) bright-field image insert in Fig. 3 shows the α and β-phase regions. The α-phase is observed to contain a significant dislocation density indicative of solidification-induced thermal stresses. In contrast, Fig. 4(b) shows fine α' martensite plates typical for small volume component fabrication by SLM, where the more rapid beam scan and cooling promotes the β→α' transformation. While the larger α-phase acicular microstructure in Fig. 3 is softer (HRC 32) than the fine α-phase microstructure in Fig. 4(a), the correspondingly fine α' plates in Fig. 4(b) exhibit a hardness similar to Fig. 4(a): 41 HRC (Rockwell C-scale hardness) versus 40 HRC. Figs. 3 and 4 also demonstrate α/β, α, and α'-rich phase microstructures, respectively for relatively equiaxed, non-directional growth for either EBM or SLM fabrication in contrast to the variations in directional growth described by Thijs *et al.*[14] for SLM of Ti–6Al–4V. The TEM image in Fig. 5 shows the primarily fine-phase α for the EBM microstructure in Fig. 4(a) in contrast to the primarily α' martensite for the fine SLM microstructure in Fig. 4(b) shown in the TEM image of Fig. 6. The interfaces separating the small α grains in Fig. 5 are primarily α grain boundaries, with no β-phase. (Note dislocations within these fine α grains). The α' martensite plates in Fig. 6 are also intermixed with fine α grains, some containing deformation twins shown at T in Fig. 6 as a consequence of process-induced thermal stresses.

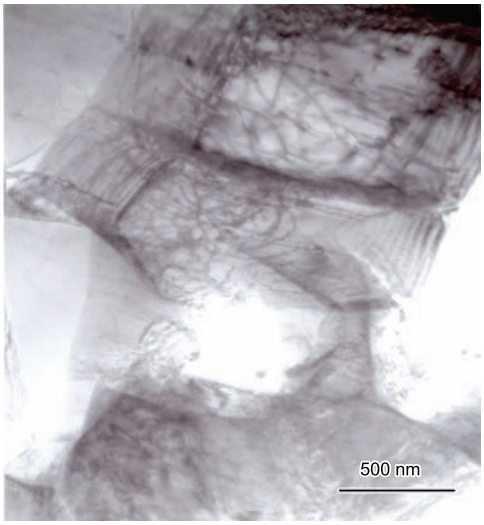

Fig. 5 TEM bright-field image showing fine α-phase microstructure corresponding to Fig. 4(a) for EBM-fabricated Ti–6Al–4V. Note dislocation substructure in α-grains

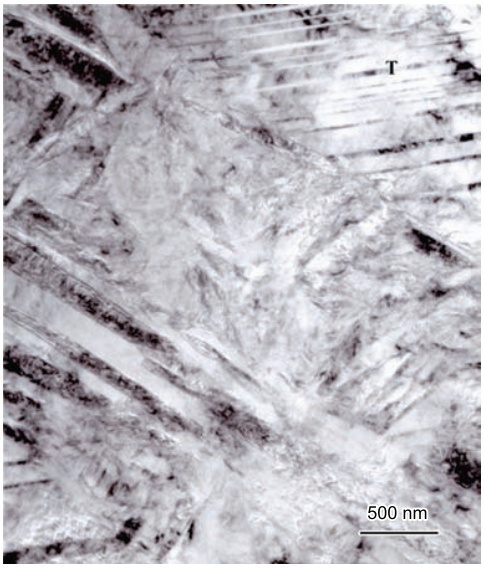

Fig. 6 TEM bright-field image showing primarily fine α'-martensite corresponding to Fig. 4(b) for SLM-fabricated Ti–6Al–4V. Note deformation twins in α-phase grain indicated at T

4. Novel Directional Microstructure in Cu Fabricated by EBM

While directional, columnar grains have been observed in Ti–6Al–4V fabricated by SLM[14], Ramirez *et al.*[17] have recently observed columnar Cu_2O precipitates in high-purity copper fabricated by EBM. Fig. 7 shows a 3D optical metallograph composite representing a section from an EBM-fabricated component illustrating these Cu_2O (cubic cuprite) precipitates which form

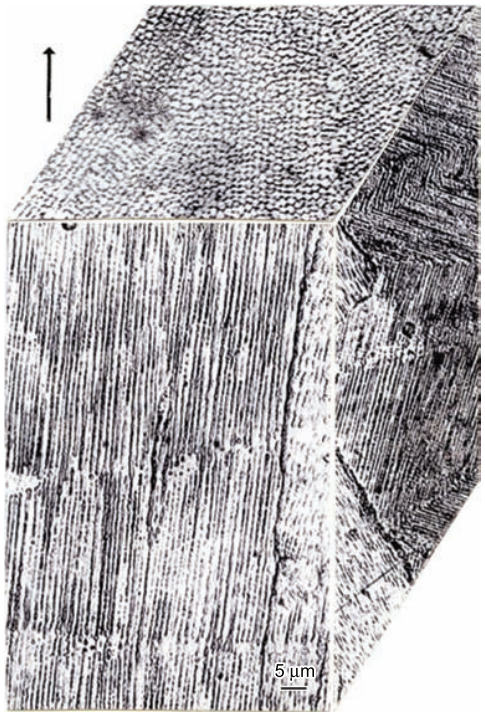

Fig. 7 3D optical microscopy composite section showing columns of Cu_2O cube precipitates in a Cu matrix component fabricated by EBM. The arrow (upper right) indicates the build direction

in the progressive melt pools which extend from each melted Cu powder layer addition, from precursor powder shown in Fig. 1(c). The magnified TEM image in Fig. 8 shows the cubic Cu_2O precipitates to be entangled with, and connected to, dislocations which presumably formed in response to thermal stresses associated with the precipitate formation and cooling in the melt pools. The selected-area electron diffraction (SAED) pattern insert in Fig. 8 illustrates the (110) orientation texture in the vertical reference plane parallel to the build direction indicated in Fig. 7.

Fig. 9 shows a simple sketch illustrating the regular melt pool geometry resulting from x-y beam scan which can characterize both EBM and SLM layer building. The melt pool dimension (Fig. 9), which may conceptually apply for the EBM Cu fabrication in Fig. 7, is roughly 2–3 μm, but the actual layer melt configuration does not appear to be as orthogonally regular or extensive as depicted in Fig. 9. Fig. 10 extends this orthogonal zone model in three dimensions showing the extension of melt pools creating columnar arrays of Cu_2O precipitates and dislocation arrays as shown in Figs. 7 and 8. These precipitates (Cu_2O) arise from oxygen absorbed during Cu atomization in purified Ar as a consequence of the affinity for oxygen of finely atomized Cu powder particles. Optical microscopy examination of the interior of atomized Cu precursor powder as in Fig. 1(b) has shown Cu_2O precipitates at grain boundaries and these precipitates either reform (solutionize) or are reorganized

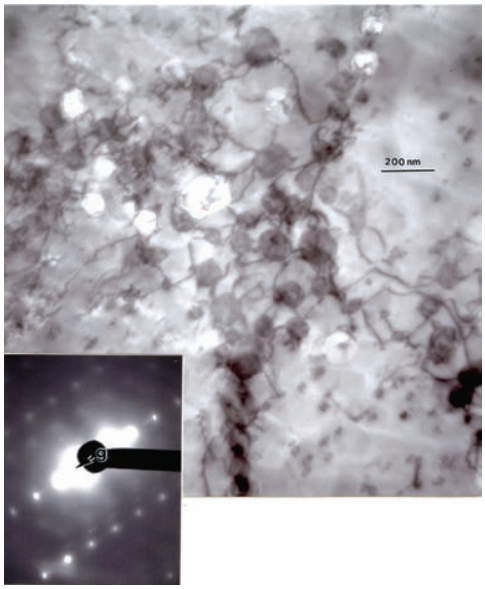

Fig. 8 TEM bright-field image showing Cu_2O precipitates and associated dislocation structure (arrows) in the vertical reference plane in Fig. 6. The white areas are etched out precipitates. The SAED pattern insert shows the (110) surface orientation. The operating reflection, **g**, is $[00\bar{2}]$

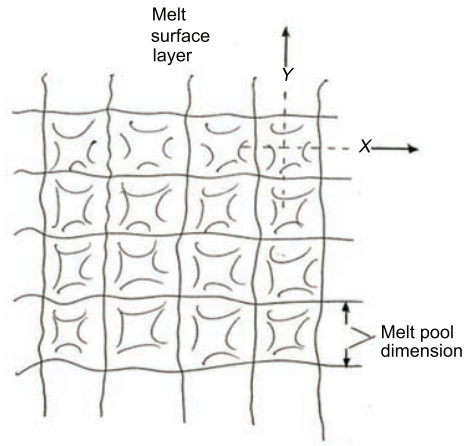

Fig. 9 Schematic view of powder (layer) bed perpendicular to the build direction. x–y denotes the orthogonal melt beam scan. The beam parameters (beam diameter, scan spacing, energy density, *etc.*) determine the melt pool dimension

within the melt pool structures creating columnar precipitate architectures shown in Fig. 7, and rendered more schematically in Fig. 11. Fig. 11(a) also shows, in addition to precipitate columns, columnar or directionally oriented (textured) grains which can exhibit a directional orientation in the horizontal reference plane in a fabricated section perpendicular to the build direction (Fig. 1(a) and (b)) (shown as $[HKL]H$ in Fig. 11(a)). This texture can also be observed as a vertical reference plane texture parallel to the build direction as shown by $[HKL]V$ in Fig. 11(a);

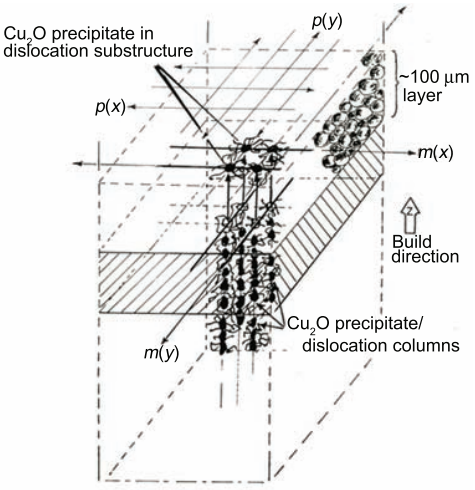

Fig. 10 Schematic model for development of Cu_2O precipitates in continuous melt zones created by x–y electron beam scanning in EBM of Cu precursor powder (Fig. 1(c)). Beam scan $p(x)$–$p(y)$ correspond to x–y in Fig. 9. (From Ramirez *et al.*[17])

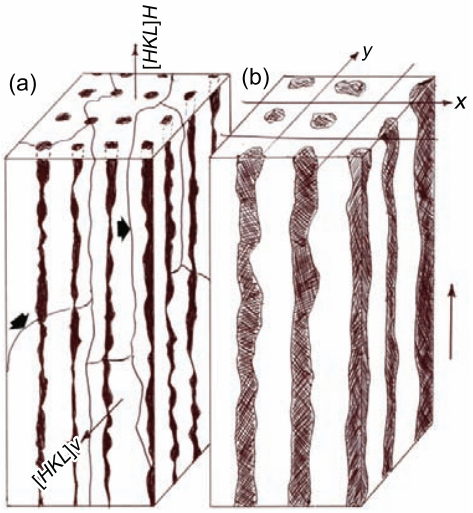

Fig. 11 Schematic models showing directional microstructure (elongated, oriented grains) and columnar microstructural architecture (a) oriented in the build direction at B. (b) shows columnar microstructural architecture corresponding to Fig. 7 and Fig. 9. The large arrows in (a) show columnar grain boundaries

depending upon the preparation of the vertical section. That is, the grinding and polishing can produce a variety of orientations relative to the build direction. Fig. 11(b) shows the columnar architecture development associated ideally with the continuous melt zones referenced to the ideal surface schematic shown in Fig. 9. The extension of each melt pool is often considered as a form of continuous epitaxy, especially for continuous, directional columns or elongated grains.

Unlike solidification from a large melt volume

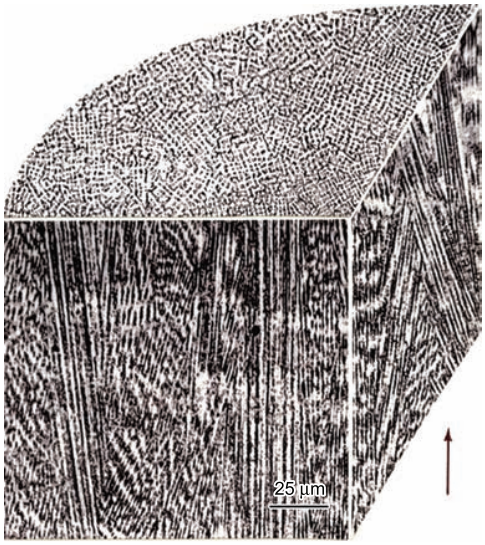

Fig. 12 3D-optical microscopy image composite section view for alloy 625 component fabricated by EBM. The build direction is noted by the arrow (lower right). Ni_3Nb bct precipitate columnar arrays are spaced ∼2–3 μm

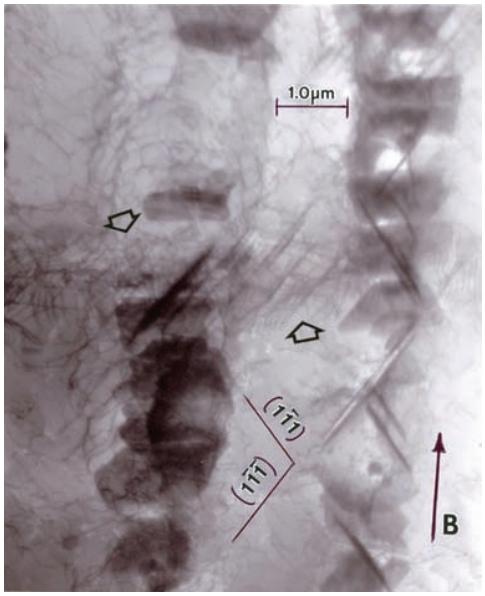

Fig. 13 TEM bright-field image showing Ni_3Nb bct precipitate plates coincident with NiCr fcc {111} planes noted. The vertical reference plane view corresponds to Fig. 12. The section (grain) surface orientation is (110). Note dislocation substructure associated with the precipitates as in Fig. 8 (small arrows). The arrow marked B indicates the build direction

where the solid/liquid interface velocity defines the rate of solidification[18], the scan speed and beam energy density in melting successive layers in either the EBM or SLM systems are controlling, and connected in melt profiles represented ideally in Fig. 9. As noted previously, this can allow for process manipulation at microscopic levels, and the ability to control both microstructures and novel microstructural architectures implicit in Fig. 7.

5. Columnar Precipitate Architectures in a Ni-Base Superalloy (Inconel 625) Fabricated by EBM and SLM

Fig. 12 shows a 3D optical metallograph composite illustrating a columnar precipitation architecture similar to Fig. 7 for a Ni-base superalloy (Inconel 625: 66Ni-21Cr-9Mo-4Nb in weight percent) fabricated by EBM. The columnar precipitates, shown in the enlarged TEM image in Fig. 13, have been identified as γ''-Ni_3Nb bct platelets coincident with the NiCr fcc matrix {111} planes[19] as illustrated in Fig. 13. Correspondingly, the NiCr matrix grains evident in the horizontal plane of the 3D composite view in Fig. 12 exhibit a [200] texture in the horizontal plane, and parallel to the build direction ($[HKL]H$=[200] in Fig. 11(a)) and a [220] ([110]) texture in the vertical reference plane as shown in the vertical reference plane TEM image in Fig. 13; which corresponds to $[HKL]V$ in Fig. 11(a) ($[HKL]V \equiv [110]$ in Fig. 13). Similar precipitation and grain orientations (textures) were observed by Strondl *et al.*[20] for EBM fabricated Inconel 718 components, while more recent observations of columnar γ''- Ni_3Nb (bct) precipitates in Inconel 718 fabricated by SLM appeared identical to the 3D optical metallograph composite in Fig. 12, although the γ'' precipitate platelets were coincident with the NiCr fcc matrix {001} planes rather than the {111} planes as shown in Fig. 13[21].

Fig. 14 shows, in comparison with Fig. 12, that SLM fabrication of Inconel 625 from pre-alloyed, atomized precursor powder also produces components having similar columnar precipitate architecture composed of γ''-Ni_3Nb (bct) precipitates in the NiCr-fcc matrix (a=0.356 nm). While Fig. 14 is a magnified composite view in contrast to Fig. 12, it can be observed that the columnar NiCr grain sizes in the horizontal reference plane are similar, and XRD spectra show the orientation is [200]. The columnar precipitate spacing of ∼2 μm in Fig. 14 is slightly less than that observed in the EBM fabricated component in Fig. 12.

6. Columnar Carbide Precipitates Produced in a Co-Base Superalloy Fabricated by EBM

Gaytan *et al.*[22] have shown that a Co-base superalloy fabricated from the pre-alloyed precursor powder shown in Fig. 2, by EBM, exhibits $Cr_{23}C_6$ carbides in columnar architectures as shown for EBM fabricated Cu in Fig. 7; and the EBM and SLM fabricated Ni-base superalloy product shown in Figs. 12 and 14, respectively. Fig. 15 shows a 3D optical micrograph composite for an EBM-fabricated Co-base superalloy. The insert in Fig. 15 is a bright-field TEM image

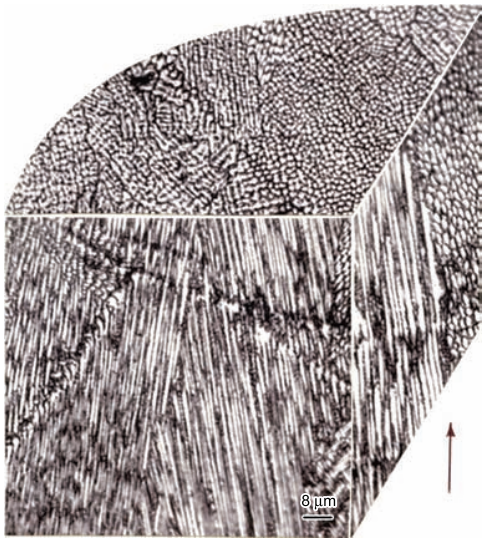

Fig. 14 3D-optical micrograph composite section view for an alloy 625 component fabricated by SLM. The columnar microstructural architecture is composed of Ni_3Nb bct plates

Fig. 15 3D-optical micrograph composite section view for a Co-base superalloy component fabricated by EBM. The columnar microstructural architecture is composed of $Cr_{23}C_6$ cubic precipitates shown in the magnified 3D TEM insert

which shows the cubic morphology for the columnar carbide (nano) precipitates (fcc; a=1.066 nm). These carbides form from the 0.2%C in the fcc CoCr matrix (a=0.355 nm) within the melt pool columns similar to the Cu_2O cubic precipitates forming in Cu as shown in Fig. 7. The regularity of the carbide architecture is implicit from the horizontal plane section microstructure shown in Fig. 15. This microstructural architecture is characteristic of the columnar arrays shown schematically in Fig. 11(b).

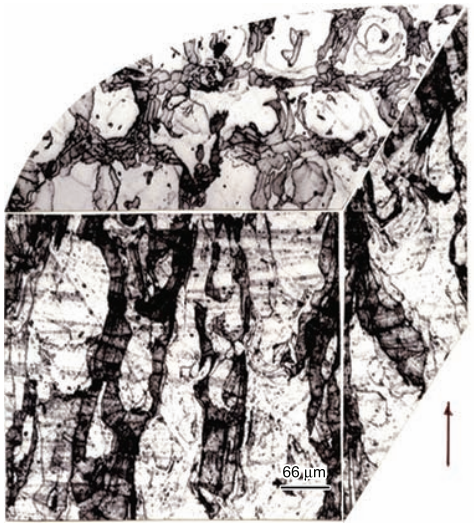

Fig. 16 3D-optical micrograph composite section view for 17-4PH stainless steel nitrogen atomized powder fabricated in argon gas (N_2-Ar) fabricated by SLM. The build direction is shown by arrow at lower right

7. SLM Fabrication of 17-4PH Stainless Steel

17-4PH stainless steel (15–17.5Cr, 3–5Ni, 3–5Cu, <1Mn, Si, 0.15–0.45 Nb, balance Fe in weight percent) has been widely used along with related precipitation-hardened (PH) stainless steels for structural and power plant applications at low service temperatures (<300 °C) since 1959[22]. Simple temper anneal at 482 °C (900 °F), referred to as an H900 temper (for 1h), produces unusual bcc Cu precipitates[23] in a martensitic (α-Fe, bcc) matrix which nominally raises the hardness by nearly 45% relative to untempered martensite; or by 100 percent relative to austenite. Jerrard *et al.*[24] and Facchini *et al.*[25] have recently fabricated 17-4PH stainless steel by SLM and observed the occurrence of metastable austenite or mixtures of austenite (fcc, a=0.357 nm) and martensite (bcc α-ferrite (Fe), a=0.286 nm) to compose the microstructure for fabricated products.

In more recent work of Murr *et al.*[26], illustrated in the 3D optical metallograph image composite in Fig. 16 (corresponding to Figs. 7, 12, 14 and 15), SLM fabrication of 17-4PH stainless steel components in an argon cover gas, produced directional martensite (bcc) oriented in the [200]α direction, parallel to the build direction shown by the arrow in Fig. 16, for either argon or nitrogen-atomized powder. The XRD (X-ray diffraction) spectra corresponding to Fig. 16, as shown in Fig. 17, illustrate the orientation features for the irregular martensite lath-like columnar grains composing the microstructure in Fig. 16: [200]α in the horizontal reference plane and [100]α in the corresponding vertical reference plane parallel to the build direction. In contrast to Fig. 16, Fig. 18

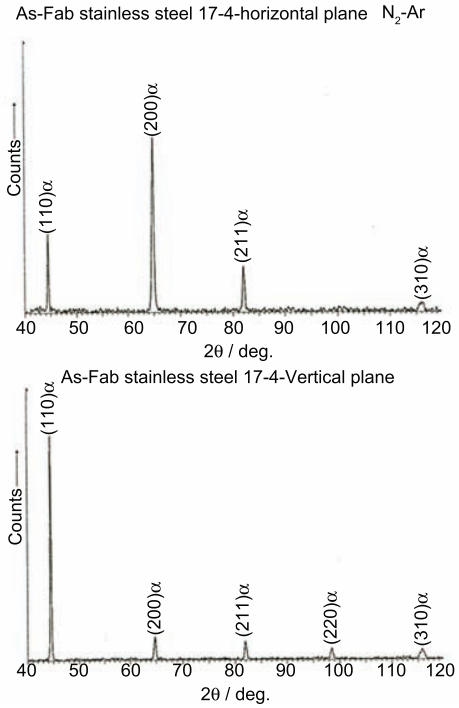

Fig. 17 X-ray diffraction (XRD) spectra corresponding to the horizontal (top) and vertical (bottom) reference planes corresponding to Fig. 16. The vertical reference plane is parallel to the build direction

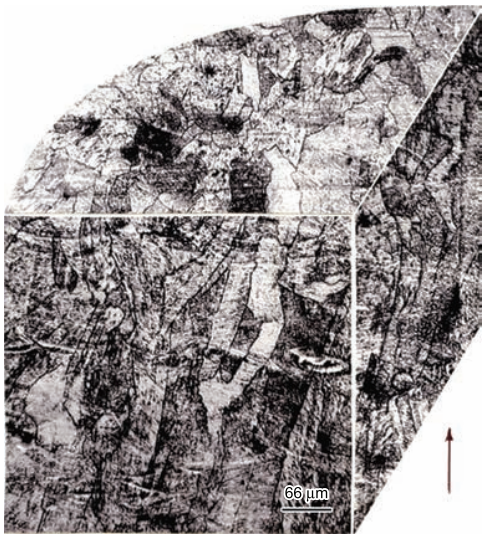

Fig. 18 3D-optical micrograph composite section view for 17-4PH stainless steel nitrogen atomized powder fabricated in nitrogen gas (N_2-N_2) by SLM. The build direction is shown by arrow at lower right

illustrates that changing the build gas environment from argon to nitrogen has a dramatic effect on the product microstructure for nitrogen-atomized precursor powder. While Fig. 18 illustrates some aspects of directional growth in the vertical reference plane, the corresponding XRD spectra in Fig. 19 shows this microstructure to be primarily austenite (γ-Fe), in

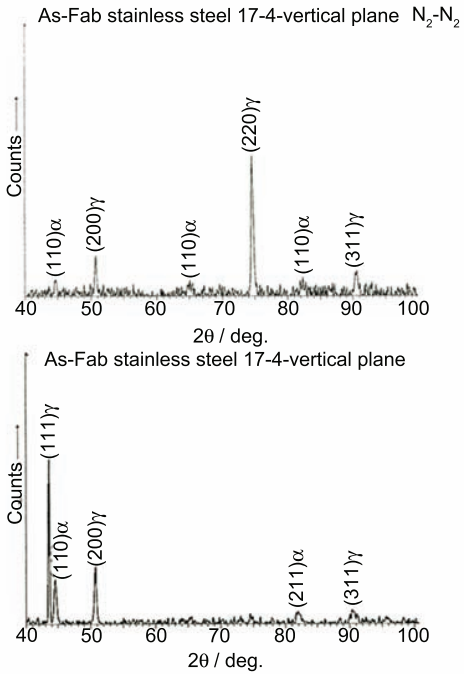

Fig. 19 X-ray diffraction (XRD) spectra corresponding to the horizontal (top) and vertical (bottom) reference planes corresponding to Fig. 18. The vertical reference plane is parallel to the build direction

contrast to martensite (α-Fe) for powder-based products built in argon. The measured hardness for the martensitic product in Fig. 16 was HRC (Rockwell C-scale hardness) 32 in comparison with primarily austenite in Fig. 18 where the hardness was ∼45% lower (HRC 22)[26]. The XRD spectra in Fig. 19 show horizontal and vertical reference plane (parallel to the build direction in Fig. 18 texturing: [220]γ and [111]γ, respectively.) This is in contrast to [200]α and [110]α for argon environment fabrication (Figs. 16 and 17).

As indicated previously, SLM build gas variations can have a dramatic effect since the conductivity of nitrogen gas is 40 percent higher than argon over a wide temperature range[9]. The ability to fabricate single and mixed phase compositions of alloys represented by 17-4PH stainless steel by SLM as shown in Figs. 16 and 18 emphasizes the processing spectrum available through electron or laser beam additive manufacturing by selecting appropriate scan strategies as discussed by Thijs *et al.*[14] In a broader context, as demonstrated on comparing Figs. 7, 12, 14–16 and 18, SLM and EBM pose the prospect for producing metal products with novel, controlled microstructural architectures. This feature, combined with the ability to fabricate complex and correspondingly multifunctional materials systems, places SLM and EBM at the forefront of advanced manufacturing technologies, especially for small specialty products and fixtures. This feature is illustrated in the next (and concluding) section which presents some examples of EBM-fabricated open cellular structures.

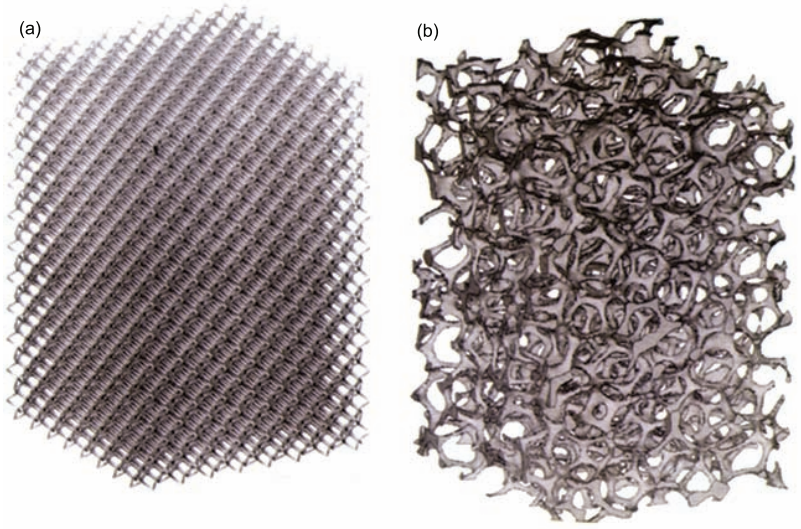

Fig. 20 CAD models for EBM or SLM fabrication of open-cellular structures. (a) Dode-thin (Materialize^{TM}) Software element-based mesh model. (b) Stochastic foam model based on micro-CT scan element

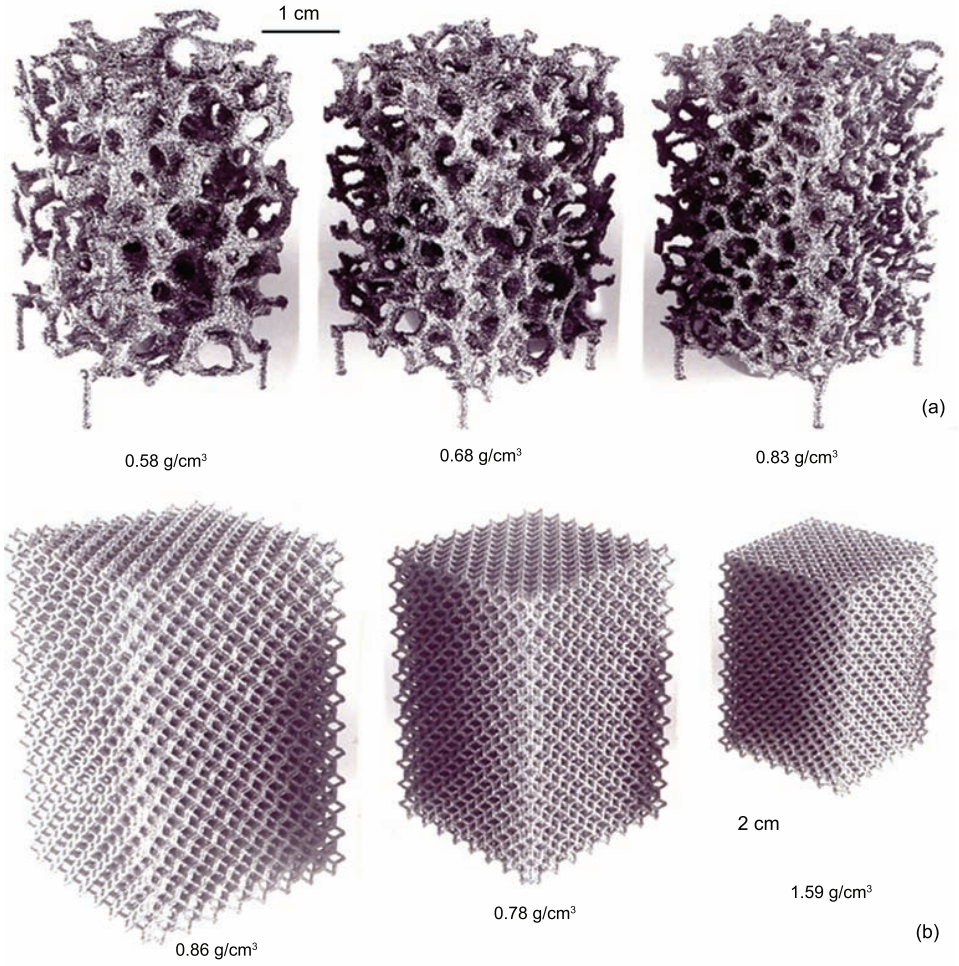

Fig. 21 EBM-fabricated foam (a) and mesh (b) structures of Ti–6Al–4V. Corresponding densities are noted

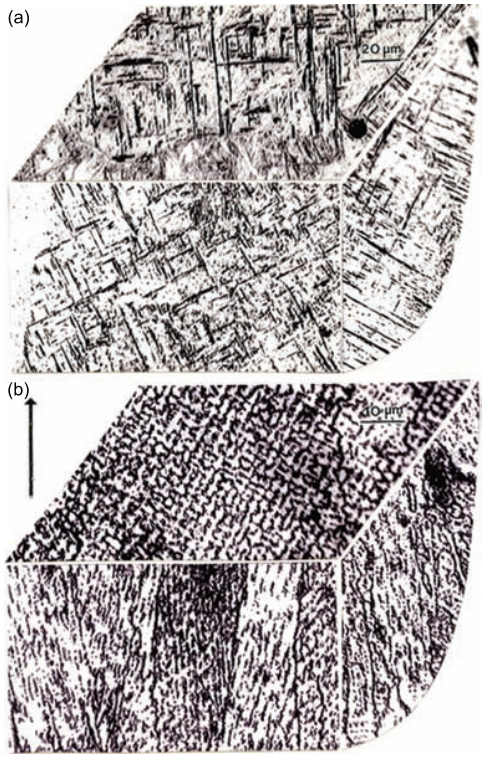

Fig. 22 3D-optical micrograph section composites for struts of mesh structures fabricated by EBM. (a) Ti-6Al-4V. (b) Co-26Cr-6Mo-0.2C. Arrow at left denotes the build direction

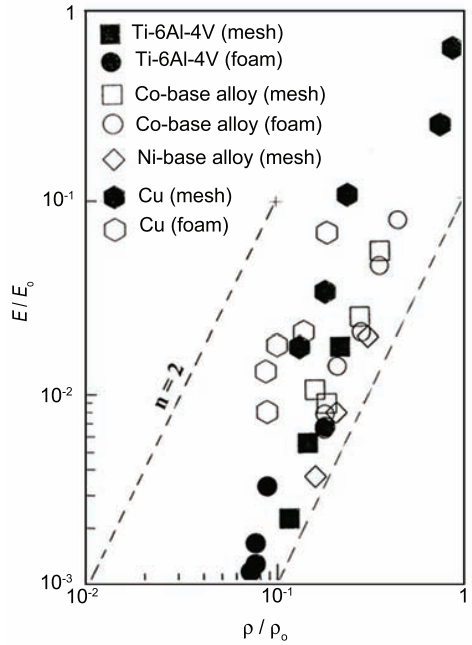

Fig. 23 Relative stiffness (E/E_o) versus relative density (ρ/ρ_o) for open cellular structures fabricated by EBM. Slope of 2 corresponding to Eq. (1) is noted. Ti–6Al–4V data from[6]; Cu data from[17]; Co-base and Ni-base alloy data from[29]

8. Application Examples for Open-Cellular Structures of Metals Fabricated by EBM

Utilizing a variety of available software packages, as well as computed tomography (CT)-scan generated model units, a number of open-cellular reticulated mesh and stochastic foam structures have recently been fabricated by EBM for Ti–6Al–4V[6,27], Cu[28], Ni and Co-base superalloys[29], and gamma-TiAl[30]. Fig. 20 illustrates model examples for a reticulated mesh and a stochastic foam. In Fig. 20(a), a geometrical unit cell or lattice structure unit has been replicated to generate the 3D-spatial model which can be embedded in CAD to selectively melt metal powder layers to create a product having any desired geometry. By expanding the lattice structure unit or varying the corresponding strut dimensions, the porosity or density can be systematically adjusted. Similar features can be achieved for stochastic foam structures represented typically in Fig. 20(b) where foam cell size and ligament dimension variations can also allow similar selectivity in product density which can be embedded in CAD models applicable in either EBM or SLM processing. Fig. 21 illustrates examples of these open-cellular structures for Ti–6Al–4V fabricated by EBM, creating density variations as indicated.

Fig. 22 shows 3D optical metallograph image composites representing typical mesh component microstructures for Ti–6Al–4V (Fig. 22(a)) and a Co-base alloy (Fig. 22(b)) identical to that represented in Fig. 15. Fig. 22(a) shows a primarily $\alpha\prime$-martensite microstructure for Ti–6Al–4V consistent with Fig. 4(b) for SLM fabrication of Ti–6Al–4V. However, this illustrates the rapid solidification/cooling effect even for EBM of small volume features such as struts and ligaments for low-density open-cellular structures illustrated in Fig. 21. Fig. 22(a) in fact corresponds to Fig. 21(b) for Ti–6Al–4V EBM processing.

Since it is difficult if not impossible to fabricate open cellular structures from many metal or alloy systems (such as Ti–6Al–4V, TiAl, Co-base alloys, *etc.*) using conventional microcasting or sintering technologies[29,32], EBM or SLM processing affords a unique manufacturing avenue to create these complex structures for any pre-alloyed precursor powder. A particularly novel application involves the manufacture of open-cellular structures with pre-selected elastic modulus or stiffness (E) for aerospace structural components, even complex heat exchangers, *etc.*, and orthopaedic implants tailored to eliminate bone stress shielding by reducing E for high-modulus metals (such as Co-base alloys where E=210 GPa) by more than an order of magnitude.

Gibson and Ashby[31] and Gibson[32] have demonstrated that open-cellular structures in general are characterized by

$$E = E_o(\rho/\rho_o)^2 \quad (1)$$

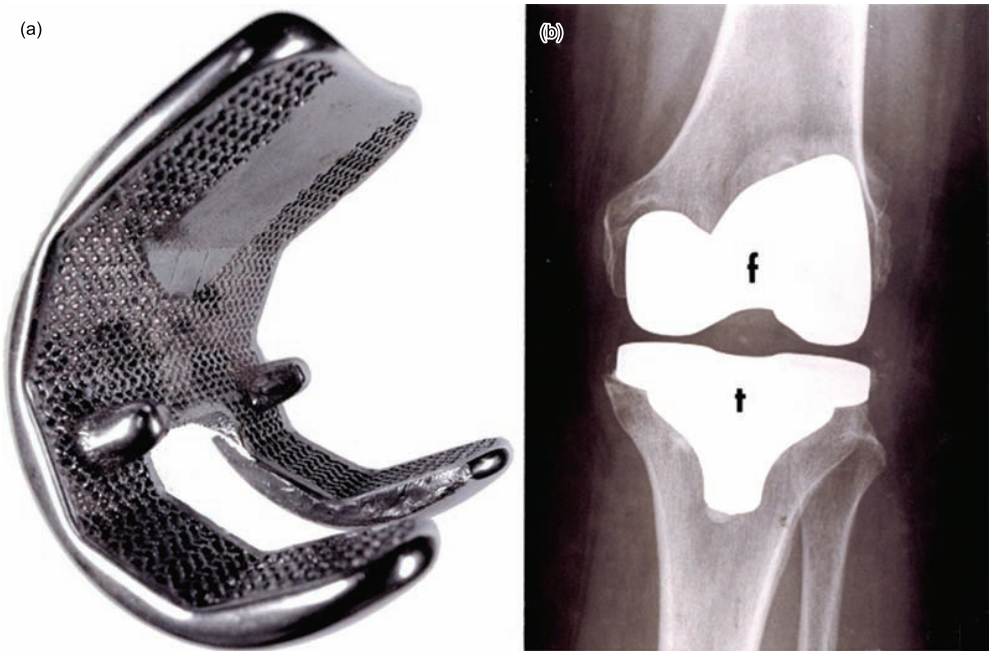

Fig. 24 Orthopaedic (knee) implants. (a) EBM-fabricated and partially finished Co-base femoral implant. Note surface mesh to contact the prepared femoral bone surface (arrow). (b) X-ray showing total knee replacement components. f indicates a Co-base (femoral) appliance while t indicates a Ti–6Al–4V tibial appliance. These are standard cast or wrought products cemented into the respective bones

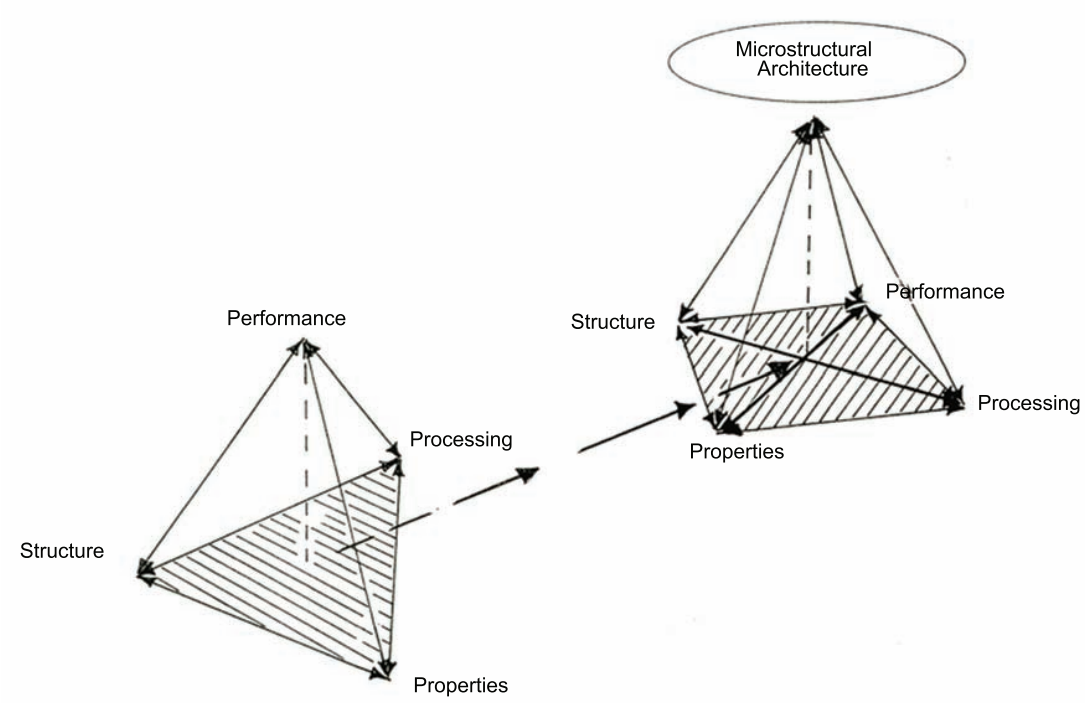

Fig. 25 Extension of the conventional materials science and engineering tetrahedron representing connections between material structure-properties-processing-performance to a new pyramid paradigm; including microstructural architectures through processing opportunities afforded by EBM and SLM fabrication

where E is the Young′s modulus or stiffness for the open-cellular structure with a density ρ, while E_o and ρ_o are the corresponding stiffness and density for a solid, fully dense structure. Fig. 23 shows a plot of relative stiffness (E/E_o) versus relative density (ρ/ρ_o) corresponding to Eq. (1) for a number of metals and alloy mesh and foam components fabricated by EBM, and using dynamic stiffness measurement techniques for determining E[6,29].

Murr *et al.*[33] have recently demonstrated how data illustrated in Fig. 23 can serve as a design strategy for biomedical (orthopaedic) implant fabrication where open-cellular structures are integrated into solid appliance manufacture promoting stiffness compatibility. These porous structures also enhance biocompatibility, including enhanced bone cell ingrowth; providing implant stabilization by eliminating adhesive cementing which is currently common practice for orthopaedic implant surgeries. Fig. 24 illustrates this concept for an experimental femoral implant fabricated from Co-base pre-alloyed powder (Fig. 2) by EBM. The interior mesh fabricated as a functional component of the implant in Fig. 24(a) corresponds to a stiffness of ∼3.4 GPa for a density, ρ=1.9 g/cm^3, or a relative density, ρ/ρ_o, of 0.2 in the Co-base mesh data plotted in Fig. 23.

Fig. 24(a) also points up several unique advantages of EBM and SLM additive manufacturing technologies. These include the ability to fabricate complex, functionally-graded structures impossible to achieve in conventional, monolithic product development, the elimination of roughly 85 percent product waste in conventional forming, machining, and finishing because unused powder is recycled (Fig. 1(a) and (b)), and the ability to create application specific or patient specific (biomedical) products through CT and micro-CT scanning to produce model-embedded CAD programs/software[6,34]. These features can be achieved by developing a range of applicable beam scan/build strategies illustrated broadly in this brief review.

9. Conclusions

Additive manufacturing using EBM and SLM processing is a new concept for metal fabrication from pre-alloyed, atomized precursor powders which has emerged since the introduction of commercial systems less than a decade ago. In this paper we have reviewed and compared some prominent examples of SLM and EBM-fabricated metal or alloy components which point up the unique features of these technologies, especially the prospects for creating metal or alloy products with controlled microstructural architectures. This could fundamentally alter or extend the traditional materials science and engineering paradigm relating structure-property-processing (synthesis)-performance in a tetrahedron to a pyramid including microstructural architecture as illustrated schematically in Fig. 25.

As recently noted by Lu[35], "metals are still the major workhorse of our society and will remain so in the future...". Indeed, additive manufacturing technologies utilizing EBM and SLM fabrication of complex, multi-functional, monolithic products of contemporary and advanced metals or alloys pose the prospect for advanced modular manufacturing, or specialty metal product manufacturing using complex CAD models. This is already being realized in many parts of the world.

Acknowledgements

This work was supported in part by Mr. and Mrs. MacIntosh Murshison Endowments at the University of Texas at El Paso and Lockheed Martin Aeronautics. We are grateful to Shane Collins of Directed Manufacturing, Austin, TX for supplying some SLM and EBM specimens examined in this comparative study. Dr. S.J. Li of IMR-Shenyang and colleagues also provided some dynamic stiffness measurements for open-cellular components.

REFERENCES

[1] C.K. Chuna, K.F. Leong and C.S. Lim: *Rapid Prototyping: Principles and Applications*, 2nd edn, World Scientific, Singapore, 2003.

[2] J. Beaman, J.W. Barlow, D.L. Bourell, R.H. Crawford and H.L. Marcus: *Solid Freeform Fabrication: A New Direction in Manufacturing*, Kluwer Academic Publishers, Dordrecht, 1997.

[3] P.F. Jacobs: *Rapid Prototyping and Manufacturing: Fundamentals of Stereolithography*, Mc Graw-Hill, New York, 1993.

[4] L. Lu, J. Fuh and Y.S. Wong: *Laser Induced Materials and Processes for Rapid Prototyping*, Kluwer Academic Publishers, Dordrecht, 2001.

[5] D.G. Poitout: *Biomechanics and Biomaterials in Orthopaedics*, Springer, New York, 2004.

[6] L.E. Murr, S.M. Gaytan, F. Medina, H. Lopez, E. Martinez, B.I. Machado, D.H. Hernandez, L. Martinez, M.I. Lopez, R.B. Wicker and J. Bracke: *Phil. Trans. Roy. Soc. A*, 2010, **368**, 1999.

[7] E.F. Bradley (Ed.): *Superalloys*, ASM International, Materials Park, OH, 1998.

[8] L.E. Murr, E. Martinez, S.M. Gaytan, D.A. Ramirez, B.I. Machado, P.W. Shindo, J.L. Martinez, F. Medina, J. Wooten, D. Ciscel, U. Ackelid and R.B. Wicker: *Metall. Mater. Trans. A*, 2011, **42**, 3491.

[9] F.M. Faubert and G.S. Springer: *J. Chem. Phys.*, 1972, **57**, 2333.

[10] M. Niinomi: *Metall. Mater. Trans. A*, 2011, **32**, 477.

[11] M. Niinomi: *J. Mech. Behavior Biomed. Mater.*, 2008, **1**, 30.

[12] J.D. Currey: *Bones: Structure and Mechanics*, Princeton University Press, Princeton, NJ, 2002.

[13] R. Ding, Z.X. Guo and A. Wilson: *Mater. Sci. Eng. A,* 2002, **327**, 233.

[14] L. Thijs, F. Verhaeghe, T. Craeghs, J. VonHumbeeck and J.P. Kruth: *Acta Mater.*, 2110, **58**, 3303.

[15] L.E. Murr, E.V. Esquivel, S.A. Quinones, S.M. Gaytan, M.I. Lopez, E.Y. Martinez, F. Medina, D.H. Hernandez, E. Martinez, S.W. Stafford, D.K. Brown, T. Hoppe, W. Meyers, U.L. Lindhe and R.B. Wicker: *Mater. Charact.*, 2009, **60**, 96.

[16] L.E. Murr, S.A. Quinones, S.M. Gaytan, M.I. Lopez, A. Rodela, E.Y. Martinez, D.H. Hernandez, E. Martinez, F. Medina and R B. Wicker: *J. Mech. Behavior Biomed. Mater.*, 2009, **2**, 20.

[17] D.A. Ramirez, L.E. Murr, E. Martinez, D.H. Hernandez, J.L. Martinez, B.I. Machado, F. Medina, R.B. Wicker and P. Frigola: *Acta Mater.*, 2011, **59**, 4088.

[18] B. Chalmers: *The Principles of Solidification*, Wiley, New York, 1964.

[19] L. E. Murr, E. Martinez, S M. Gaytan, D.A. Ramirez, B.I. Machado, P.W. Shindo, J.L. Martinez, F. Medina, J. Wooten, D. Ciscel, U. Ackelid and R.B. Wicker: *Metall. Mater. Trans. A*, 2011, **42**, 3491.

[20] A. Strondl, R. Fischer, G. Frommeyer and A. Schneider: *Mater. Sci. Eng. A*, 2008, **480**, 138.

[21] K.N. Amato, S.M. Gaytan, L.E. Murrr, E. Martinez, P.W. Shindo, J. Hernandez, S. Collins and F. Medina: *Acta Mater.,* 2012, in press.

[22] D.C. Ludwigon and A.M. Hall: *Physical Metallurgy of Precipitation Hardenable Stainless Steel*, Office of Technical Services, U.S. Dept. of Defense, Washington, D.C. (Code PB 15 1067), 1959.

[23] M. Murayama, Y. Katayama and K. Huno: *Metall. Mater. Trans. A*, 1999, **30**, 345.

[24] P.G.E. Jerrard, L. Hao and K.E. Evans: *J. Manuf. Eng.*, 2009, **223**(11), 1409.

[25] L. Facchini, N. Vicente, Jr., I. Lonardelli, E. Magalini, P. Robotti and A. Molinari: *Adv. Eng. Mater.*, 2010, **12**(3), 184.

[26] L.E. Murr, E. Martinez, J. Hernandez, S. Collins, K.M. Amato, P.W. Shindo and S.M. Gaytan: to be published, 2012.

[27] P. Heinl, L. Müller, C. Körner, R.F. Singer and F.A. Müller: *Acta Biomater.*, 2008, **4**, 1536.

[28] D.A. Ramirez, L.E. Murr, S.J. Li, Y. Tian, E. Martinez, J.C. Martinez, D.I. Machado, S.M. Gaytan, F. Medina and R.B. Wicker: *Mater. Sci. Eng. A*, 2011, **528**, 5379.

[29] L.E. Murr, S.J. Li, Y.X. Tian, K. Amatio, E. Martinez and F. Medina: *Materials*, 2011, **4**, 782.

[30] J. Hernandez, L.E. Murr, S.M. Gaytan, E. Martinez, F. Medina and R.B. Wicker: *Metallography, Microstruct.& Analysis*, 2012, in press.

[31] L.J. Gibson and M.F. Ashby: *Cellular Solids*: *Structure and Properties*, Cambridge Univ. Press, New York, 1997.

[32] L.J. Gibson: *Ann. Rev. Mater. Sci.*, 2000, **30**, 191.

[33] L.E. Murr, S.M. Gaytan, E. Martinez, F. Medina and R.B. Wicker: in *Frontiers in Bioscience; Encyclopedia of Bioscience*, 2011, in press

[34] O.L.A. Harrysson and D.R. Cormier: Chap. 9: in *Advanced Manufacturing Technology for Medical Applications:Reverse Engineering Software Conversion and Rapid Prototyping,* ed I. Gibson, John Wiley & Sans, Ltd., London, 2005, 191.

[35] L. Lu: *Science*, 2010, **328**, 319.